Energy Advances

ROYAL SOCIETY OF CHEMISTRY

PAPER

View Article Online
View Journal | View Issue

Cite this: *Energy Adv.*, 2023, 2, 1843

Design and analysis of a $SnS_2/WS_2/V_2O_5$ double-heterojunction toward high-performance photovoltaics

Jubair Al Mahmud,[a] Md. Ferdous Rahman,*[ab] Abdul Kuddus,*[c] Md. Hasan Ali,[a] A. T. M. Saiful Islam,[d] Md. Dulal Haque,[e] Sheikh Rashel Al Ahmed,[f] Muhammad Mushtaq[g] and Abu Bakar Md. Ismail[b]

Tungsten disulfide (WS_2) transition metal dichalcogenide (TMDC) absorber-based solar cells comprising tin disulfide (SnS_2) buffer and vanadium (V) oxide V_2O_5 back surface field (BSF) layers have been designed and analyzed using a SCAPS-1D simulator in this study. The initial experimentation on back metal contact (BMC) and front metal contact (FMC) optimization involved the use of different materials to obtain the least resistive junction at the semiconductor–metal (M–S) interface, where the best potential was found. Following an extensive investigation nickel (Ni) and aluminum (Al) is determined to be the optimal material for the back and front contact, respectively. Subsequently, the impact of major parameters which affecting the photovoltaic (PV) performance, such as absorber layer thickness, doping concentration, bulk defect density, interface defect density, operating temperature, and surface recombination velocity, were studied systematically. An improved photoconversion efficiency (PCE) of over 32% (around 9% higher) was obtained with the open-circuit voltage (V_{OC}) of 1.1 V, short-circuit current (J_{SC}) of 37.2 mA cm^{-2}, and fill factor (FF) of 84% with the Al/FTO/SnS_2/WS_2/V_2O_5/Ni heterostructure, compared to 23.4%, 0.89 V, 31.2 mA cm^{-2} and 81% for the pristine cell (without V_2O_5 BSF). These outcomes obtained from comprehensive studies reveal the huge potential of the $SnS_2/WS_2/V_2O_5$ double-heterostructure to be applied as a PV cell and pave a resourceful pathway for the experimental fabrication of WS_2-TMDC absorber-based high-performance photonic devices.

Received 25th May 2023,
Accepted 8th September 2023

DOI: 10.1039/d3ya00231d

rsc.li/energy-advances

1. Introduction

Energy demand is increasing quickly with the increase in population and rapid development of technology around the world; thereby, the predicted energy consumption is estimated to be 30 terawatts in 2050.[1–3] Scientists and researchers are highly concerned with the reduction of existing fossil fuel resources, their annual rate of price increment, and their dangerous impact on global warming, leading to the depletion of the ozone layer and air pollution.[4–8] Renewable energy derived from natural sources is abundant and sustainable, with the least impact on the environment. Solar energy, especially using photovoltaic technology, has the greatest potential, with the direct conversion of solar energy into electricity with a clean, economical, and sustainable pathway playing a key role in mitigating the global energy demand.[9–12] Transition-metal dichalcogenides (TMDCs) used in thin-film solar cells are one of the most attractive absorber materials for use in photovoltaic devices.[13–18] To date, there are several absorber semiconductors, including perovskites such as $FeSi_2$, Sb_2S_3, Sb_2Se_3, MoS_2, $MoSe_2$, WS_2, SnS_x, Cu_2MnSnS_4, $CsSnCl_3$, Cs_2BiAgI_6, $CsPbBr_3$, Sr_3NCl_3, and Sr_3AsI_3, that show considerable potential to be used for fabricating high-performance solar cells.[4–8] The choice of a favorable semiconductor as solar absorber material is a crucial issue to achieve the highest benefits, including inexpensive active materials, vacuum-free deposition, suitability for mass production, and markedly efficient power conversion.[13,19–21] However, the challenges in fabricating highly

[a] *Advanced Energy Materials and Solar Cell Research Laboratory, Department of Electrical and Electronic Engineering, Begum Rokeya University, Rangpur 5400, Bangladesh. E-mail: ferdousapee@gmail.com*
[b] *Solar Energy Laboratory, Department of Electrical and Electronic Engineering, University of Rajshahi, Rajshahi 6205, Bangladesh*
[c] *Ritsumeikan Global Innovation Research Organization, Ritsumeikan University, Shiga 525-8577, Japan. E-mail: kuddus4910@gmail.com*
[d] *Department of Electrical and Electronic Engineering, Bangabandhu Sheikh Mujibur Rahman Science and Technology University, Gopalganj 8100, Bangladesh*
[e] *Department of Electronics and Communication Engineering, Hajee Mohammad Danesh Science and Technology University, Dinajpur-5200, Bangladesh*
[f] *Department of Electrical, Electronic and Communication Engineering, Pabna University of Science and Technology, Pabna 6600, Bangladesh*
[g] *Department of Physics, University of the Poonch Rawalakot, Rawalakot, 12350, AJK, Pakistan*

efficient solar cells based on these materials include the use of rare-earth materials, scarcity, and material toxicity.[19,20,22–24] Additionally, the development of heterostructured devices with band alignment fulfilling the criteria of an ideal required band structure to absorb the major portion of incident visible photons and thereby generation of electron–hole pairs, their dissociation, and collection efficiency at the external circuit, is still a challenge for high-performance photovoltaics beyond the Shockley–Queisser (SQ) limit.[13,19–21]

The WS_2 layered material has emerged as a promising one to be used as an absorber material, with an optical absorption coefficient exceeding 10^5 cm^{-1}, a tunable gap of 1.3–2.1 eV for bulk and monolayer film, and the high carrier mobility of 486 cm^2 V^{-1} s^{-1} (at 5 K), while being much less hazardous and relatively abundant.[25] Therefore, the choice of WS_2 as a solar cell absorber may benefit the manufacture of inexpensive thin-film solar cells.[26–31] The n-type electron transport layer (ETL), *i.e.*, the buffer layer, has a vital impact on the cell's open-circuit voltage and short-circuit current density. The band alignment at the absorber/buffer interface *i.e.*, band offset which is specially (CBO) determines the band bending at the interface is a spike that inhibits recombination. SnS_2 is known as a low-cost, n-type layered semiconductor with nontoxic nature, having the tunable bandgap of 1.82–2.88 eV and electron mobility of 50 cm^2 V^{-1} s^{-1}.[21] Several numerical and experimental studies report the use of WS_2 as a solar cell photoactive material, with multiple heterostructures demonstrated.[29–36] The PCE of 5.0% with 625 nm exposure and a power density of 2.5 mW cm^{-2} for the Au(10 nm)/WS_2(20 nm)/Ag(200 nm) structure,[37] and 0.31% with V_{OC} of 0.551 V, J_{SC} of 1.01 mA cm^{-2}, and FF of 47.6% for the ITO/WS_2 structure, have been obtained.[32,33] However, the improved PCE of 17.73% for Al:ZnO/WSSe/WS_2/TCO,[30] 25.71% in AZO/ZnO/WS_2/Mo,[35] 28.86% for n-TiO_2/p-WS_2/p-Cu_2O,[38] and 29.74% for ZnO/CdS/WS_2/Au[34] heterostructures are predicted by developing double heterojunction structures. These theoretical outcomes reveal that the limited V_{OC} obtained in WS_2-based photovoltaics are observed mostly owing to the Fermi level pinning, which could be solved by adding an interlayer (back surface field [BSF] layer) between WS_2 and the back metal contact, establishing a suitable band alignment with the least carrier recombination.[31,39–41] Also, the smooth transfer of holes from the absorber to the back metallic contact is facilitated by the low valence band offset with a highly doped p-type BSF.[42] Thus, the PCE could be enhanced effectively by reducing the valence band offset at the BSF/absorber interface, consequently developing a high activation energy that is almost equal to the absorber's band gap.[43,44] Moreover, some inorganic metal oxides (MOs) such as vanadium pentoxide (V_2O_5), nickel oxide (NiO), and tungsten trioxide (WO_3) have been incorporated as a BSF layer in numerous structures to enhance both cell performance and stability.[45,46] Among them, p-type V_2O_5 (2.2 eV) showed promising features as BSF material, with moderate band gap, strong absorption coefficient, significant conductivity, and huge versatility, with abundance on Earth.[11] With this perspective, the double junction heterostructure of SnS_2/WS_2/V_2O_5 with WS_2 absorber, SnS_2 buffer and V_2O_5 BSF layer shows a favorable band alignment required for spontaneous carrier transportation with insignificant offsets (CBO at the SnS_2/WS_2 interface of ~0.19 eV and VBO at WS_2/V_2O_5 of ~0.26 eV), revealing its notable potential with nontoxic, low-cost and green characteristics for developing high-performance photovoltaics.

In this work, transition-metal dichalcogenide WS_2-absorber-based high-performance thin film solar cells (TFSCs) with SnS_2 and V_2O_5 as buffer and back surface field (BSF) layers, respectively, have been designed and analyzed using the SCAPS-1D simulator. Firstly, the influence of various possible metals as back contact was investigated to obtain the least resistive junction at the semiconductor–metal (M–S) interface. After that, the impacts of major affecting parameters such as absorber layer thickness, doping density, defect density, interface defect density, operating temperature, and its back surface recombination velocity with the buffer and BSF layers were investigated. A comprehensive simulation study reveals the huge potential of WS_2, SnS_2, and V_2O_5 as an absorber, buffer, and back surface field (BSF) layer, respectively, for the fabrication of high-performance economical and green thin film solar cells (TFSCs).

2. Device modeling and simulation parameters

The realization of high-efficiency solar cells can be obtained by numerical modeling and a systematic investigation of the role of each influential parameter of the designed cells. The one-dimensional electrical solar cell simulation software SCAPS-1D developed at the Department of Electronic and Information Systems at the University of Ghent in Belgium has shown potential to design and analyze TFSCs. Optoelectrical simulations of PV device structures consisting of up to seven semiconductor layers can be carried out using the SCAPS-1D software. The optoelectronic properties of PV cell structures can be predicted and analyzed by applying fundamental equations, as well as electrostatic potential and continuity equations, under steady-state conditions.[47]

Fig. 1(a)–(d) shows the schematic diagram and corresponding energy band alignment with and without V_2O_5 BSF of the proposed thin-film solar architectures. In the adjusted heterostructure with V_2O_5 BSF of Al/FTO/SnS_2/WS_2/V_2O_5/Ni, p^+–p–n–n^+ junctions are formed with a p-type 1.0 μm WS_2 absorber layer sandwiched between the highly doped p^+-type 0.1 μm V_2O_5 BSF and n-type 0.05 μm SnS_2 buffer layer. The FTO (0.05 μm) layer is used as a transparent conductive oxide (TCO) layer along with the back metal contact. In the energy band diagram simulation for the architecture of Al/FTO/SnS_2/WS_2/V_2O_5/Ni, the energy levels (both VB and CB) of the p-type V_2O_5 BSF layer and the n-type SnS_2 buffer layer are notably higher than those of the WS_2 absorber layer. The difference in the energy levels of the conduction band (CBO) between the BSF and the absorber is determined to be 0.91 eV, which facilitates the easiest path for transporting the photogenerated holes (PGHs), and conversely, it blocks photogenerated electrons

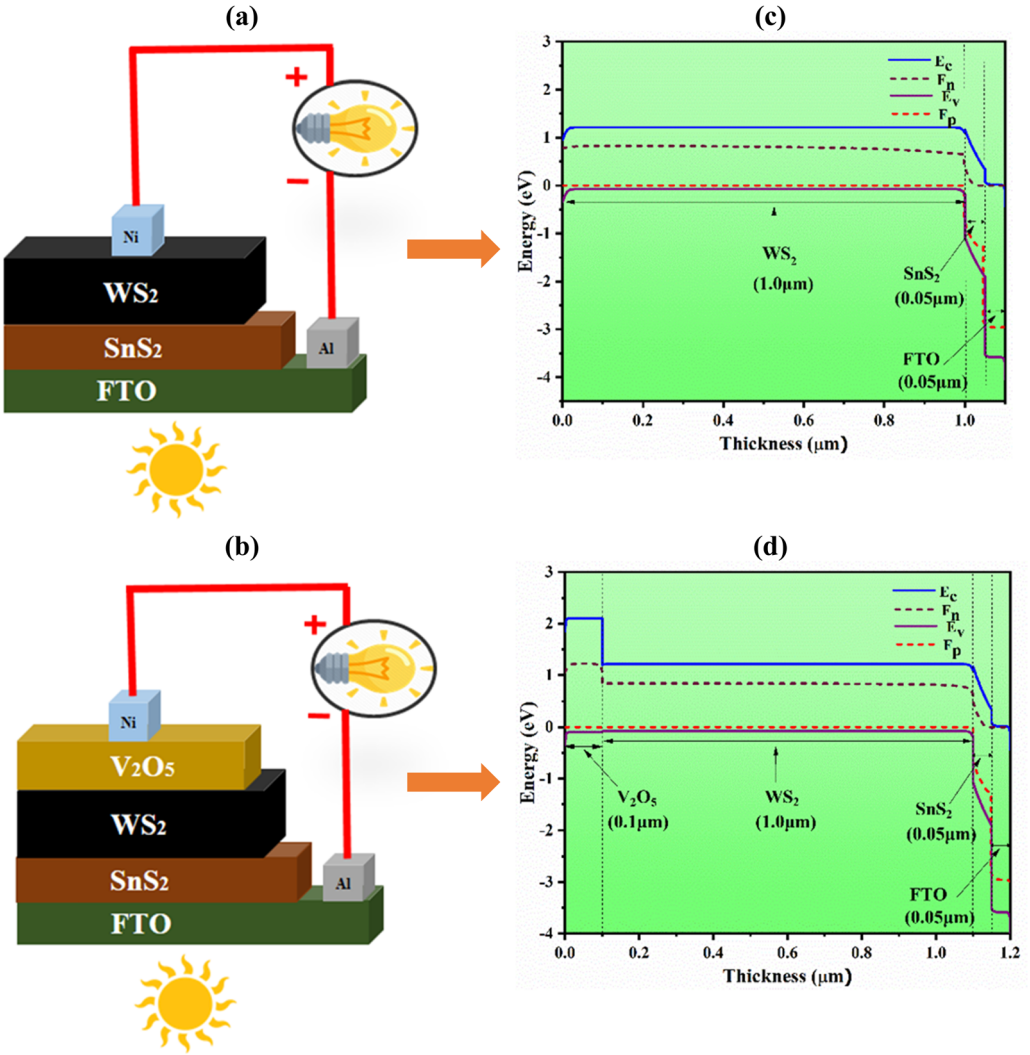

Fig. 1 (a) and (b) Schematic diagram and (c) and (d) corresponding energy band alignment with and without V_2O_5 BSF of the proposed heterostructures.

(PGEs) passing into the back contact Ni (5.01 eV). The difference in the energy levels of the conduction band (CBO) between the buffer and the absorber is determined to be 0.95 eV. This energy difference accelerates the transport of photogenerated electrons (PGEs) and inversely repels the way of photogenerated holes (PGHs) into the front contact.

In the SCAPS-1D simulator, the fundamental equations of one-dimensional semiconductors, Poisson's equation, hole and electron continuity equations, as well as the drift and diffusion drift eqn (1)–(5)[48–51] have been calculated to determine the PV parameters. The Poisson and continuity equations provide a set of coupled differential equations (Ψ, n, p) or (Ψ, E_{Fn}, E_{Fp}) with correct boundary conditions at interfaces and contacts. In this simulator, the intrinsic properties of each layer, such as layer thickness (nm); band gap E_g (eV); electron affinity χ (eV); dielectric permittivity ε_r; states density of the conduction band N_C (cm^{-3}); density of the valence band N_V (cm^{-3}); electron mobility μ_n ($cm^2\ V^{-1}\ s^{-1}$); hole mobility μ_p ($cm^2\ V^{-1}\ s^{-1}$); donor density N_D (cm^{-3}); acceptor density N_A (cm^{-3}); recombination coefficients ($cm^3\ s^{-1}$) of radiative recombination, Shockley–Read–Hall recombination (SRH) and Augur recombination; and the absorption coefficient, are required to be provided from experimental outcomes as well as reported literature. The simulation was performed under AM 1.5G standard spectrum.

In this simulator, the absorption coefficient of each photoactive layer/material is required to be provided separately to simulate any homo/heterostructures from experimental results/literature, as summarized in Tables 1 and 2. The absorption coefficients of SnS_2, WS_2, and V_2O_5 were taken from reported literature.[11,13,51–54] So, this modeling and the performed simulation is reliable. However, a noticeable discrepancy between simulation and experiment may be observed when the suggested device is fabricated experimentally owing to fabrication limitations, environmental impacts and measurement errors.

$$\frac{\partial^2 \Psi}{\partial x^2} + \frac{q}{\varepsilon}\left[p(x) - n(x) + N_D + N_A + \rho_p - \rho_n\right] = 0 \qquad (1)$$

Table 1 Simulation parameters of the proposed (Al/FTO/SnS_2/WS_2/V_2O_5/Ni) solar cells

Parameter (unit)	n^+-Type TCO (FTO)[57]	n-Type buffer (SnS_2)[52,53]	p-Type absorber (WS_2)[13,54]	p^+-Type BSF (V_2O_5)[11,51]
Thickness (μm)	0.05	0.05	1.00	0.10
Bandgap (eV)	3.6	2.24	1.29	2.2
Electron affinity (eV)	4.50	4.24	4.05	3.40
Dielectric permittivity (ε_r)	10.0	10.0	13.6	8.00
CB effective density of states (cm^{-3})	2.0×10^{18}	2.0×10^{18}	2.2×10^{18}	9.2×10^{19}
VB effective density of states (cm^{-3})	1.8×10^{19}	1.8×10^{19}	1.8×10^{19}	5×10^{20}
Electron thermal velocity (cm s^{-1})	2×10^7	1×10^7	1×10^7	1×10^7
Hole thermal velocity (cm s^{-1})	1×10^7	1×10^7	1×10^7	1×10^7
Electron mobility (cm^2 V^{-1} s^{-1})	100	50	200	150
Hole mobility (cm^2 V^{-1} s^{-1})	20	25	50	100
Shallow uniform donor density N_D (cm^{-3})	1×10^{18}	1×10^{17}	—	—
Shallow uniform acceptor density N_A (cm^{-3})	—	—	1×10^{18}	1×10^{19}
Bulk defect density (cm^{-3})	—	1×10^{15}	1×10^{14}	1×10^{15}

Table 2 Interface defect parameters of the proposed (Al/FTO/SnS_2/WS_2/V_2O_5/Ni) solar cells

Parameters (unit)	V_2O_5/WS_2	WS_2/SnS_2
Defect type	Neutral	Neutral
Capture cross-section of electrons (cm^2)	1×10^{-19}	1×10^{-19}
Capture cross-section of holes (cm^2)	1×10^{-19}	1×10^{-19}
Reference for defect energy level E_t	Above the highest E_v	Above the highest E_v
Energy with respect to a reference (eV)	0.6	0.6
Total density (cm^{-2})	1×10^{11}	1×10^{10}

$$\frac{1}{q}\frac{\partial J_p}{\partial x} = G_{op} - R(x) \quad (2)$$

$$\frac{1}{q}\frac{\partial J_n}{\partial x} = -G_{op} + R(x) \quad (3)$$

$$j_n = -\frac{U_n n}{q}\frac{\partial E_{Fn}}{\partial x} \quad (4)$$

$$j_p = +\frac{U_p p}{q}\frac{\partial E_{FP}}{\partial x} \quad (5)$$

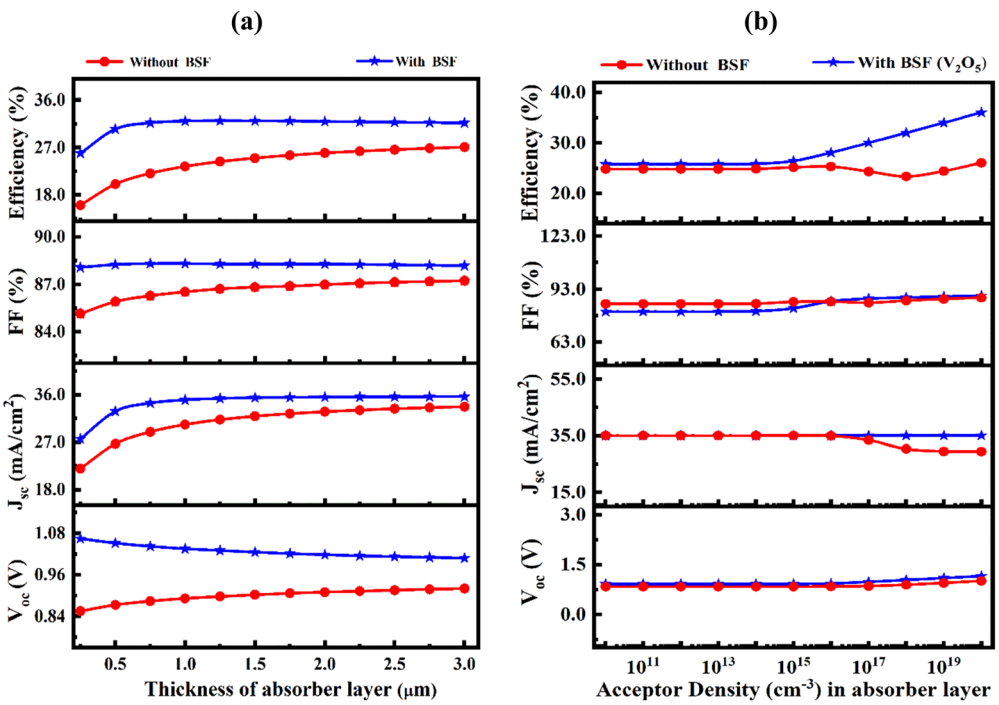

Fig. 2 Effect of absorber layer parameters: (a) thickness and (b) acceptor density with and without V_2O_5 BSF layer of the proposed heterostructure (Al/FTO/SnS_2/WS_2/Ni).

where ψ is the electrostatic potential; $\varepsilon^0\varepsilon_r$ is the vacuum and semiconductor permittivity; n and p are free carrier concentrations; and N_d^+ and N_A are ionized donor and acceptor densities. The defect charge density is denoted by ρ_{def}; G is the generation rate, and j_n and j_p are the electron–hole current densities; q is the elementary charge; U_n and U_p are respectively electron and hole recombination rate; μ_n and μ_p are electron and hole mobility, respectively.

The radiative recombination, Shockley–Read–Hall recombination (SRH) and Augur recombination were considered with recombination coefficients of 2.0×10^{-9} (cm^3 s^{-1}), 1.0×10^{14} (cm^3 s^{-1}) and 1.0×10^{-29} (cm^3 s^{-1}), respectively, in this study.

Recombination used for introducing the radiative and Auger (band-to-band) recombination in SCAPS-1D can be expressed as shown in eqn (6) and (7).[55]

$$U_{radiative} = K\left(np - n_i^2\right) \quad (6)$$

$$U_{Auger} = \left(c\frac{A}{n}n + c\frac{A}{p}p\right)\left(np - n_i^2\right) \quad (7)$$

Here, c_n^A and c_p^A can be set from literature; *i.e.*, for Si, $K_{Si} = 1.8 \times 10^{-15}$ cm^{-3} s^{-1}; GaAs, $K_{GaAs} = 7.2 \times 10^{-10}$ cm^{-3} s^{-1}; CIGS $K = 0$; and the Auger constants are: $c_n^A \approx c_p^A \approx 3.0 \times 10^{-31}$ cm^{-6} s^{-1}.[56]

Table 1 lists the simulation parameters for the active layers used for modeling and designing the proposed devices. Herein, the thermal velocity of electrons and holes in each semiconductor at room temperature is fixed at approximately 10^7 cm s^{-1} throughout the study. The chosen value for surface recombination velocity of electrons and holes at the metallic contacts located at the front and back of the structure is 10^7 cm s^{-1}. The chosen value for electron and hole capture cross-sections is 10^{-15} cm^2. The work function referring to aluminum (Al) and nickel (Ni) was used as an optimized front and back metallic contact.[13]

3. Results and discussion

3.1 Influence of thickness and carrier concentration of WS_2 absorber layer on PV performance

Fig. 2(a) displays how the performance parameters of the solar cell are influenced by changes in thickness within the range of 0.25–3.0 μm, keeping unchanged the rest of the parameters as

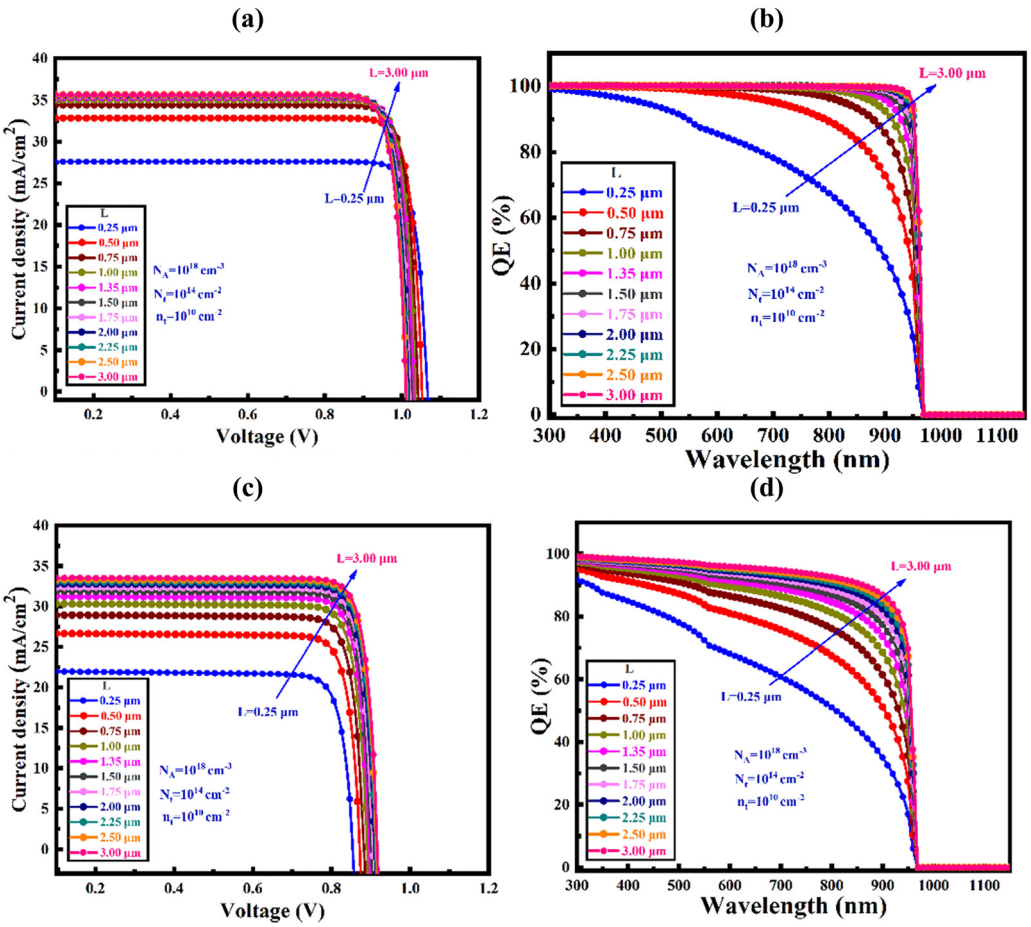

Fig. 3 Effects of absorber layer thickness on the *J*–*V* and Q–E of solar cells constructed (a) and (b) with BSF V_2O_5 and (c) and (d) without BSF V_2O_5, respectively.

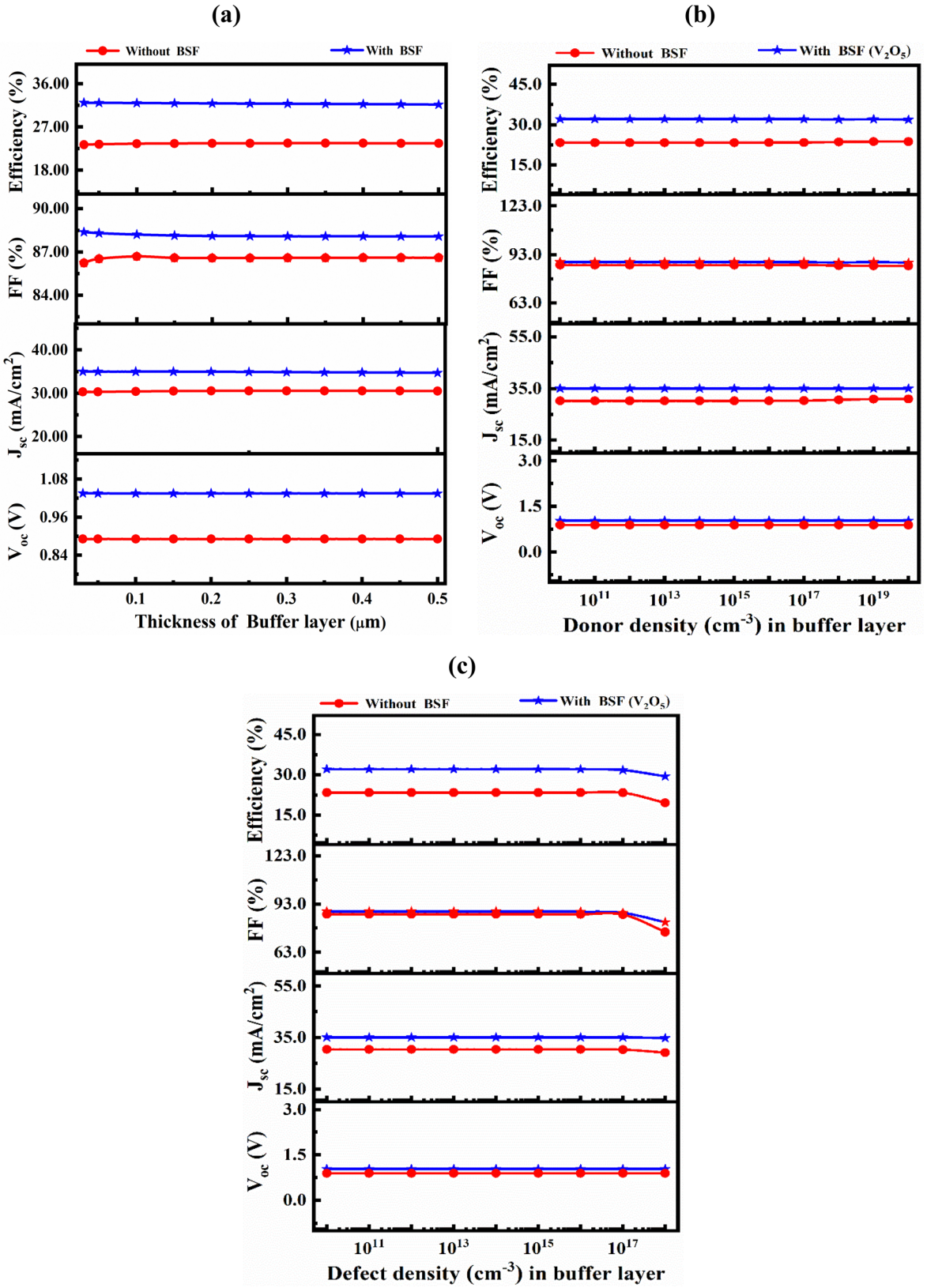

Fig. 4 Effect of varying (a) thickness, (b) donor concentration and (c) bulk defect density of the SnS_2 buffer layer in both structures with and without BSF layer.

shown in Tables 1 and 2, under AM 1.5G illumination at a constant working temperature of 300 K. The V_{OC} is significantly changed at a thin absorber thickness of $\leq$1.0 μm. A markedly improved V_{OC} (from ~0.84 to ~1.0 V) was seen in the solar cell structure with V_2O_5 BSF at the absorber thickness of 0.08–1.0 μm, which is consistent with previous reports.[40,58] The efficiency of the cell increased from 16.03% to 27.06% and 25.88% to 32.09% for the heterostructure without and with BSF layer, respectively, with an increase in absorber thickness from 0.25–3.0 μm. The J_{SC} increased almost linearly when absorber thickness was varied from 0.25–0.75 μm, and thereafter, it reached a saturated value of 35.6 (with BSF) and 33.7 mA cm^{-2} (without BSF) with further increase in absorber thickness beyond 0.75 μm. The enhancement in J_{SC} values is a consequence of the increased absorption of incident photons at higher wavelengths in the WS_2 absorber with the V_2O_5 BSF layer. Logically, an absorber with a higher thickness having BSF absorbs more photons, resulting in a greater number of electron–hole pairs (EHPs) generated.[59,60] A smaller increase in FF was found at a lower thickness of <0.75 μm, which is almost constant over the absorber thickness of up to 3.0 μm. The tendency of reduction in V_{OC} refers to the gradual increase of recombination of photogenerated carriers. This process may come to an end when the absorber thickness reaches >3.0 μm. The PCE gradually reduces (from 26 to 24%) at higher acceptor concentrations, above 10^{16} cm^{-3}, when no BSF layer is added, while the PCE increases sublinearly after insertion of the V_2O_5 BSF between the WS_2 absorber and Ni back contact.

Though the performance parameters are insignificantly changed with an increase in acceptor concentration from 10^{10} to 10^{16} cm^{-3}, surprisingly, a marked increase in PCE from 26.3% to 36.5% with FF from 77% to 81% and V_{OC} from 0.77 V to 0.81 V was observed with increasing acceptor concentration from 10^{16} to 10^{20} cm^{-3} (Fig. 2(b)). This significant improvement was obtained due to the enhancement of carrier (hole) density, resulting in the formation of a strong built-in field, which causes the improved V_{OC} as well as FF.

Fig. 3 shows the *J*–*V* characteristics and corresponding quantum efficiency (QE) response to varying absorber thicknesses from 0.25 to 3.0 μm for structures with and without the BSF layer, respectively. In Fig. 3(a), the photocurrent J_{SC} increases exponentially from 27 to 36 mA cm^{-2} with an increase of absorber thickness in the entire region of 0.25 to 0.9 μm. The corresponding QE response demonstrates the improvement of photoabsorption by expanding the area coverage (indicated by arrow) with increasing absorber thickness, which causes the resulting enhancement in J_{SC} (Fig. 3(b)). A similar characteristic was also observed in the structure without the BSF layer, having a current of 33 mA cm^{-2} and relatively smaller area of coverage in the QE response, as shown in Fig. 3(c) and (d). This is

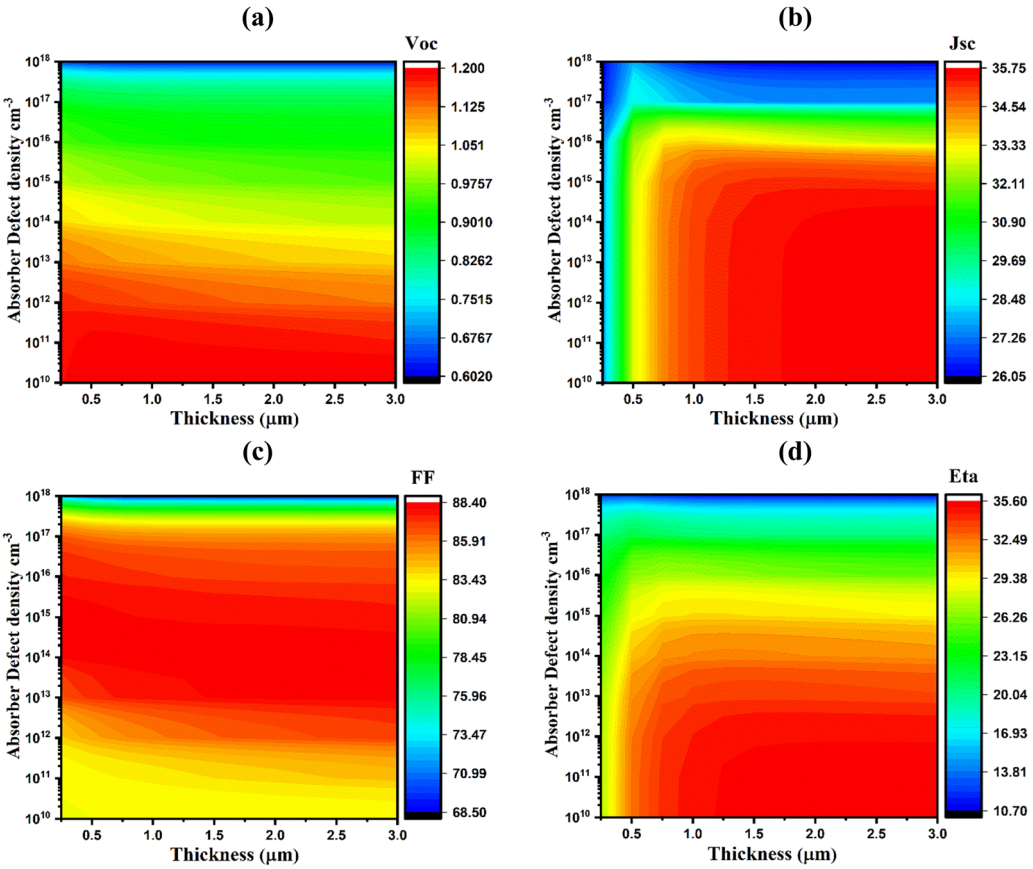

Fig. 5 Effects of WS_2 absorber thickness and bulk defect density variations on the photovoltaic parameters: (a) V_{OC}, (b) J_{SC}, (c) FF, and (d) η.

because a thicker absorber layer leads to an increase in cell resistance and diffusion length, which causes severe unwelcomed recombination of photogenerated carriers.[59,61] Thereby, the optimal absorber thickness of 1.0 μm was used for further investigation based on the adjusted photovoltaic parameter values for both configurations, resulting in the highest η of 32.02% and 23.39% achieved for the structure with and without the BSF layer, respectively.

There is a significant improvement in V_{OC} with the increase in WS_2 acceptor density from 10^{10} to 10^{20} cm^{-3}. In the case with BSF, there is a shift in the V_{OC} value from 0.918 to 1.152 V, whereas without BSF, the V_{OC} value changes from 0.84 to 1.01 V, and the conversion efficiency increases from 25.82 to 36.07% due to the variation in acceptor density from 10^{10} to 10^{20} cm^{-3}. Without the BSF layer, the J_{SC} changes from 35.01 to 29.37 V, the FF from 84.73 to 88.22%, and consequently, the conversion efficiency changes from 24.83 to 26.08% with the acceptor density variation in the range of 10^{10}–10^{20} cm^{-3}. In both cases, FF and efficiency did not show appreciable changes with acceptor density up to 10^{15} at the WS_2 absorber layer. To attain the best possible photovoltaic performance, this study has chosen the layer thickness of 1.0 μm and acceptor density of 10^{18} cm^{-3} in the WS_2 absorber layer for further investigations.

3.2 Influence of thickness, carrier concentration, and defect density variation of SnS_2 buffer layer on PV performance

Fig. 4 illustrates the variation of photovoltaic parameters of the proposed thin film heterojunctions with varying layer thickness, carrier concentration, and defect density of the SnS_2 buffer. In Fig. 4(a), PV parameters were found almost unchanged with the variation of SnS_2 buffer layer thickness from 0.03 to 0.5 μm in both structures with and without the BSF. This may be due to the thin layer thickness with higher carrier density ($\sim 10^{17}$ cm^{-3}) of the SnS_2 buffer layer. Considering an effective transmission of incident photons from SnS_2 to WS_2 absorber, a thin thickness of 0.05 μm was chosen as the optimal thickness of the SnS_2 buffer layer. Further, an insignificant change in PV parameters was observed when the carrier concentration in SnS_2 increased up to 10^{20} cm^{-3} in both structures, as depicted in Fig. 4(b). In the structure with BSF, the V_{OC}, J_{SC}, FF, and efficiency decreases from 1.035 to 1.030 V, 35.04 to 35.03 mA cm^{-2}, 88.39 to 87.92%, and 32.05 to 31.72%, respectively, while these were changed from 0.891 to 0.890 V, 30.268 to 30.960 mA cm^{-2}, 86.44 to 85.99%, and 23.32 to 23.74%, respectively, for the heterostructure without BSF.

The photogenerated electrons would have to travel farther to get to the front contact as the SnS_2 buffer layer's thickness increases, which would enhance the potential for carrier

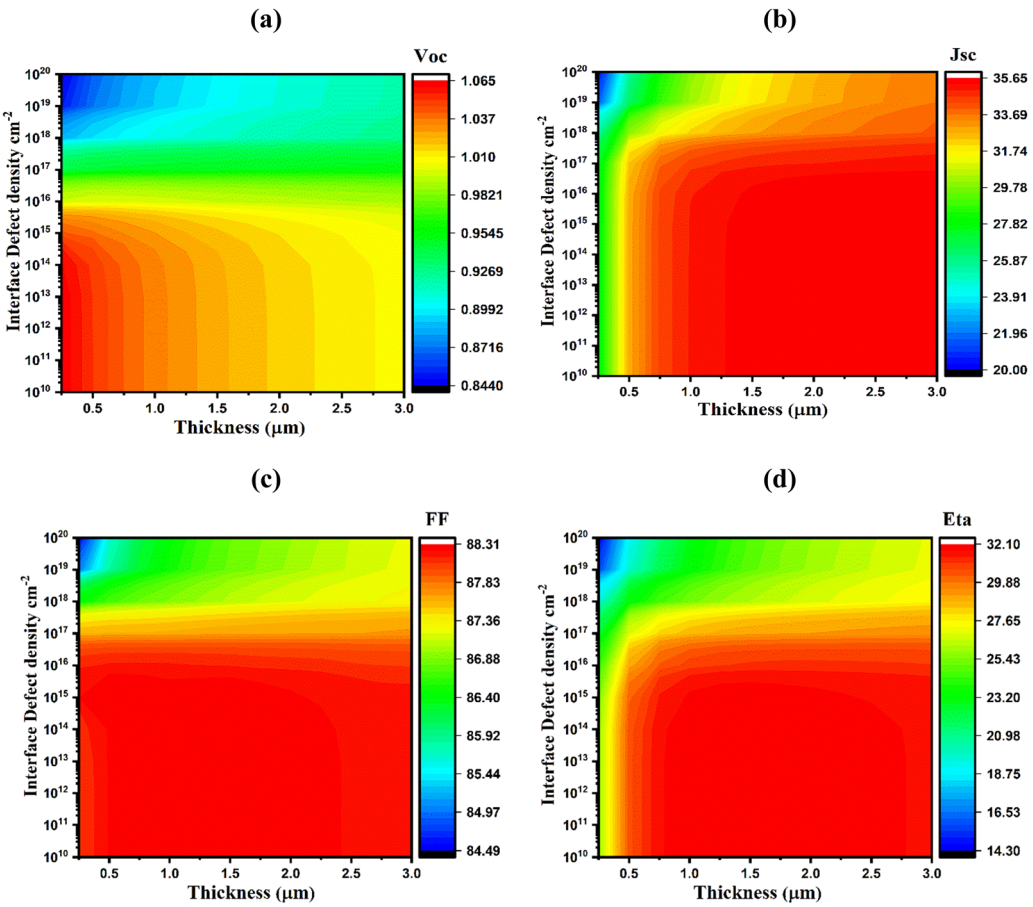

Fig. 6 Effects of absorber thickness and interface (V_2O_5/WS_2) defect density variations on the photovoltaic parameters: (a) V_{OC}, (b) J_{SC}, (c) FF, and (d) η.

recombination. Therefore, the optimum values for thickness and doping concentration were found at 0.05 μm and 10^{17} cm^{-3}, respectively, considering photon transmission and material utilization of the efficient buffer layer.

Fig. 4(c) shows the variation of PV parameters at different n-type defect densities of the SnS_2 buffer layer from 10^{10} to 10^{18} cm^{-3}, keeping unchanged the rest of the parameters. PV parameters drastically change as the bulk defect density increases from 10^{16} cm^{-3} for both scenarios with and without the BSF structure. An increase in bulk defect density in the SnS_2 layer leads to an augmentation in the rate of Shockley-Read-Hall (SRH) recombination, causing a severe deterioration in the overall performance of cells.[62] So, the optimum value of defect density should be lower than 10^{15} cm^{-3} to obtain the best performance from the proposed cells.[62] Thus, a thickness of 0.05 μm, doping concentration of 10^{17} cm^{-3}, with a defect density of 10^{15} cm^{-3} in SnS_2, are optimal for use as a potential buffer in the proposed device structures.[63]

3.3 Influence of thickness and bulk defect density variation in the WS_2 absorber layer on PV performance

Fig. 5 illustrates the variation of PV parameters corresponding to relative bulk defect density and layer thickness of the WS_2 absorber from 10^{10} to 10^{18} cm^{-3} and 0.25 to 3.0 μm, respectively. A marked reduction in solar cell parameters was found when the defect density of WS_2 exceeds 10^{14} cm^{-3} with a layer thickness of $\geq$0.5 μm. The J_{SC}, V_{OC}, FF, and PCE of cells with BSF (Al/FTO/SnS_2/WS_2/V_2O_5/Ni) decreased from 35.71 to 26.05 mA cm^{-2}, 1.2 to 0.6 V, 88.31 to 68.54%, and 35.55 to 10.78%, respectively, when the bulk defect density and absorber layer thickness were varied from 10^{10} to 10^{18} cm^{-3}. In Fig. 5(a), the highest V_{OC} of 1.0983 V is achieved when the BSF layer thickness is ~1.0 μm and defect density is $\leq 10^{14}$ cm^{-3}; however, it sharply dropped to 0.604 V at a defect density higher than this critical value (~10^{14} cm^{-3}). As shown in Fig. 5(b), the highest J_{SC} value of 35.71 mA cm^{-2} was achieved at a defect density of $\leq 10^{16}$ cm^{-3} with layer thickness larger than 1.0 μm. The FF reached the maximum value of 88.31% when defect density was less than or equal to 10^{14} cm^{-3} and layer thickness was higher than 1.1 μm, so far, and it dropped noticeably to 68.54% corresponding to a defect density beyond 10^{14} cm^{-3}, as shown in Fig. 5(c). As a result, the highest conversion efficiency, exceeding 30%, was obtained at a layer thickness of ~1.0 μm and defect density of ~10^{14} cm^{-3} (Fig. 5(d)). A high carrier recombination rate occurs across the cell as a result of the introduction of several defect states in the absorber layer, which in turn lowers cell performance.[13,64,65] Thus, the highest PCE

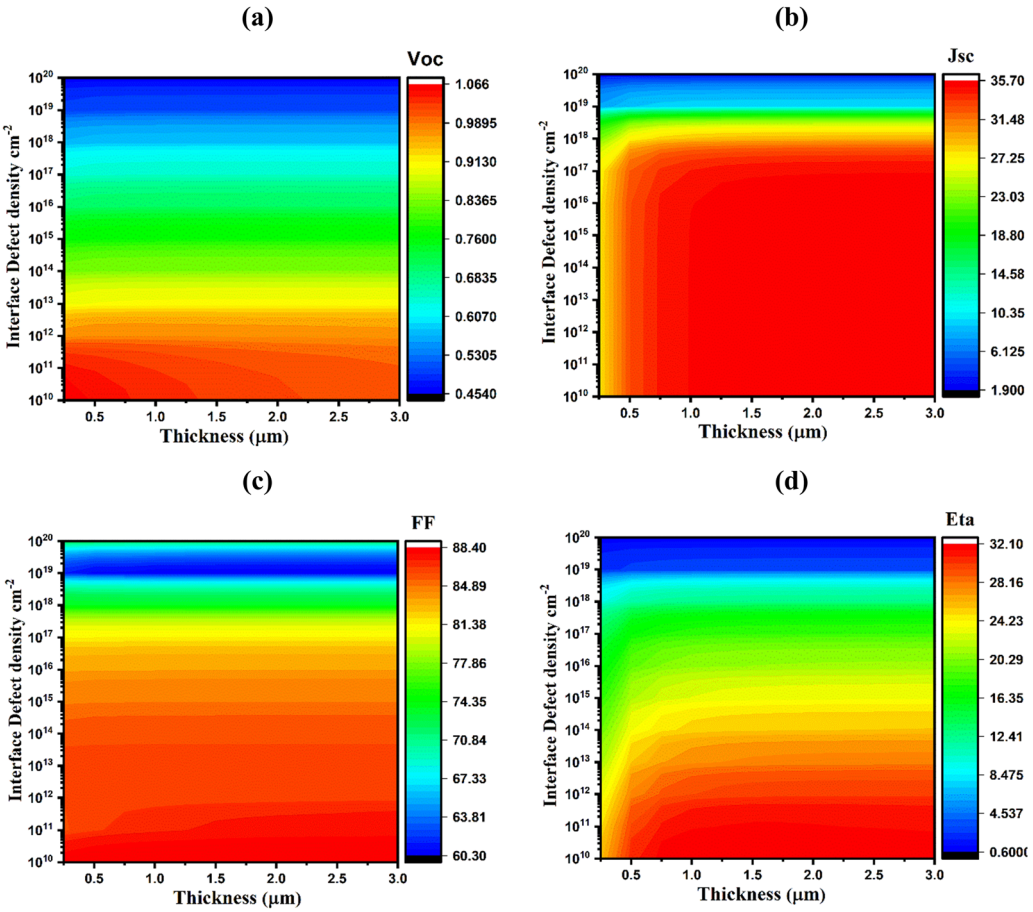

Fig. 7 Effects of absorber thickness and interface (WS_2/SnS_2) defect density variations on the photovoltaic performance parameters: (a) V_{OC}, (b) J_{SC}, (c) FF, and (d) η.

exceeding 32% with V_{OC} of 1.035 V, a J_{SC} of 35.03 mA cm^{-2}, and an FF of 88.31% were obtained at a layer thickness and bulk defect density of $\geq$1.0 μm and $\leq 10^{14}$ cm^{-3} of the WS_2 absorber, respectively.

3.4 Influence of layer thickness and interface defect density variation of the WS_2 absorber on PV parameters

The quality of the interface has a significant impact on the cell's performance and thereby plays a vital role in the interaction between light and electricity. Fig. 6(a)–(d) displays the changes in PV parameters for various interface defect densities of 10^{10}–10^{20} cm^{-2} for the V_2O_5/WS_2 interface at a thickness of 0.25–3.0 μm of the WS_2 absorber layer. The PV parameters were insignificantly affected at the interface defect density of $\leq 10^{10}$ cm^{-2}, while they were markedly decreased with an increase in interface defect densities over 10^{14} cm^{-2} for both of the V_2O_5/WS_2 interfaces. The J_{SC}, V_{OC}, FF, and PCE decreased from 35.64 to 20.04 mA cm^{-2}, 1.065 to 0.845 V, 88.31% to 84.49%, and 32.1% to 14.3% for the structure with the BSF layer, while it drastically decreased from 35.641 to 1.971 mA cm^{-2}, 1.065 to 0.455 V, 88.31% to 60.38%, and 32.09% to 0.65%, respectively, for the structure without BSF layer, which requires proper steps during practical cell fabrication to obtain the predicted optimized cell performance by tackling interface defects. Thus, the highest conversion efficiency of over 30% was achieved when the interface defect density was adjusted to $\leq 10^{16}$ cm^{-2} at a layer thickness of ~1.0 μm of WS_2 absorber.

Fig. 7(a)–(d) depicts the change of PV with varying WS_2/SnS_2 interface defect density from 10^{10}–10^{20} cm^{-2} and WS_2 absorber layer thickness of 0.25–3.0 μm. The highest V_{OC} of 1.098 V was obtained for all WS_2 thicknesses when the defect density was below 10^{11} cm^{-2}; however, it severely dropped from 1.098 to 0.464 V for the defect density beyond 10^{12} cm^{-2} (Fig. 7(a)). In Fig. 7(b), the maximum value for J_{SC} of 35.642 mA cm^{-2} was achieved at a defect density of $\leq 10^{14}$ cm^{-2} and an absorber thickness of $\geq$0.75 μm. In the meantime, the FF decreased gradually from 88.31% to 72.41% at each thickness value of the WS_2 absorber in the range of 0.25–3.0 μm and interface defect density of $\leq 10^{10}$ cm^{-2}, as shown in Fig. 7(c). As a result, the highest conversion efficiency exceeding 30% was achieved at the defect density of $\leq 10^{11}$ cm^{-2} and absorber thickness of $\geq$0.75 μm, as demonstrated in Fig. 7(d). These detailed simulation outcomes reveal that the defects formed at the WS_2/SnS_2 interface have a severe impact on solar cell performance compared to defects at the $WS_2/WS_2/V_2O_5$ interface, which is consistent with reported studies.[40,44]

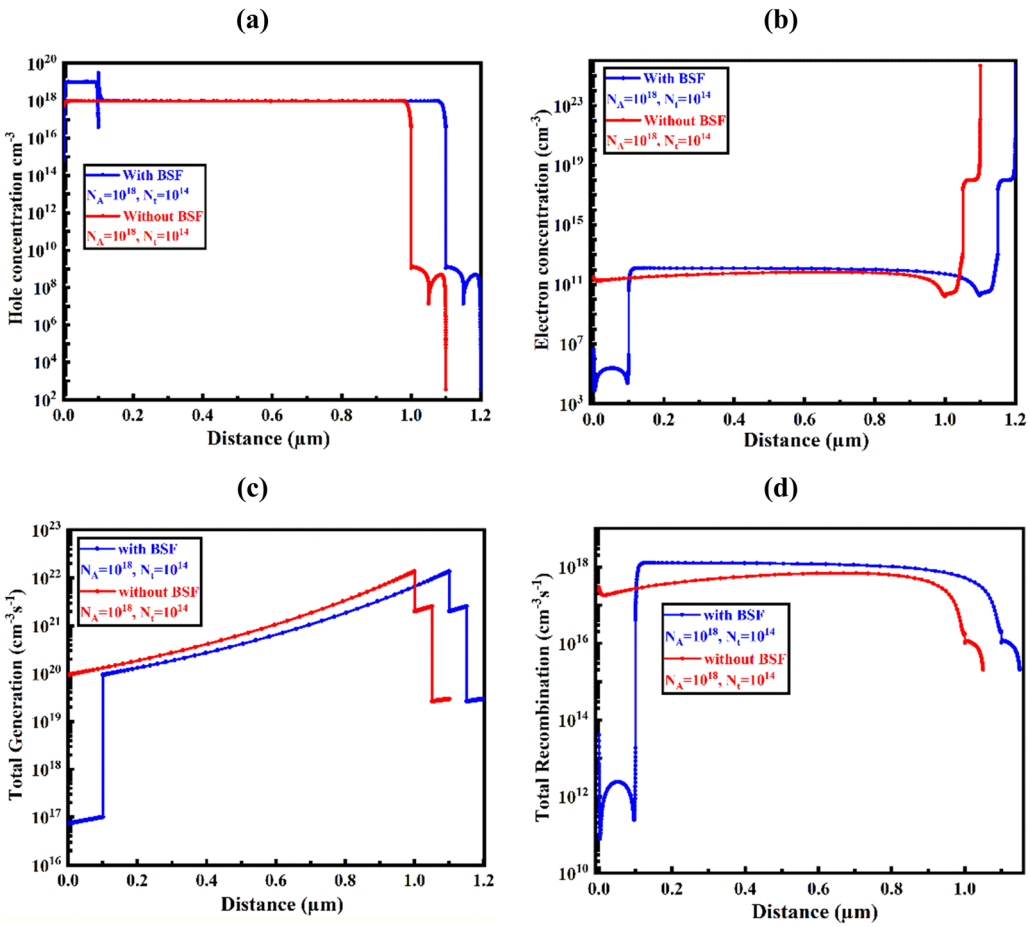

Fig. 8 Impact on (a) hole and (b) electron carrier concentration, (c) total generation, and (d) recombination of the absorber layer thicknesses.

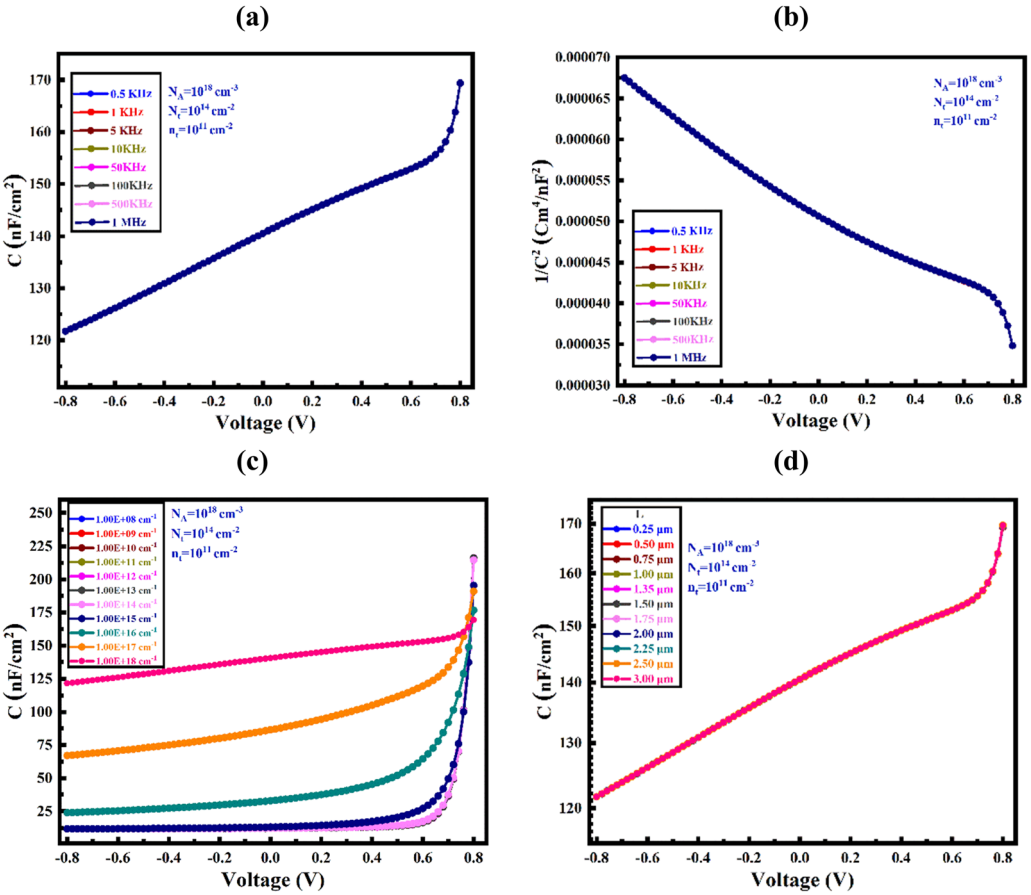

Fig. 9 (a) Impact on C–V in solar cells with varying frequency; (b) $1/C^2$–V Mott–Schottky curve; C–V curves with (c) varying absorber doping and (d) varying absorber thickness.

3.5 Influence of the absorber layer's carrier concentration on the G–R profile

Fig. 8(a)–(d) demonstrates the impact on the carrier (electron and hole) concentration and total generation–recombination (G–R) profiles in configurations with and without the BSF layer at a constant acceptor concentration N_A of 10^{18} cm^{-2} and defect density N_t of 10^{14} cm^{-2}. Regardless of whether a solar cell has a back surface field (BSF) layer or not, the carrier concentration of the absorber layer shows a noticeable effect on G–R by the incident photon. In the cell structure of the BSF layer, a higher concentration of carriers in the WS_2 absorber increased G–R recombination closer to the front surface of the cell. This happens due to an increase in available carriers at the higher carrier concentration, which leads to a rise in the rate of recombination. With a structure incorporating BSF, the impact of the carrier concentration in the absorber layer on the G–R profile is mitigated because of the formation of an aligned energy band with the least band offset among the absorber, BSF and metal contact. Because the BSF layer is designed to reduce recombination at the back surface of the cell, it can also affect the G–R profile near the front surface, which is consistent with previous reports.[66] Total (electron and hole) generation at the absorber thickness of ~1.0 μm was found to be the maximum, and on the contrary, resulted in the least total recombination loss.

3.6 Capacitance–voltage (C–V) characteristics of the proposed heterojunctions

Fig. 9 illustrates the capacitance–voltage characteristics of the proposed heterojunction solar cells over a frequency range of 0.5 kHz to 1 MHz. Conventionally, p–n junctions are linked to the development of depletion and diffusion of charges. At reverse bias voltage, the depletion capacitance surpasses the diffusion capacitance, whereas the diffusion capacitance predominates at forward bias. These C–V characteristics under a range of frequencies, absorber concentrations, and thicknesses reveal the versatility of charge modulation in the proposed WS_2-absorber-based solar cells. For a specific frequency, the capacitance increases sublinearly with the increase in polarization potential, which indicates a negligible acuity of the absorber traps at all frequencies, as shown in Fig. 9(a). Under reverse bias conditions, the existing traps are unable to mitigate the effective charge, leading to a decrease in capacitance, which is consistent with previous studies.[67,68] With increasing carrier concentration, the capacitance increases markedly, while it is absolutely amplified with increasing polarization potential. Surprisingly, the capacitance increased almost linearly with absorber thickness up to 0.8 μm.

Fig. 9(b) displays the Mott–Schottky plot of the proposed Al/FTO/SnS_2/WS_2/V_2O_5/Ni heterostructured cell. The intersection

of the $1/C^2$ plot with the voltage axis gives rise to the flat-band potential of the proposed solar cell. The p-type WS_2 layer is mostly occupied by the space charge area, as indicated by the negative slope of the plot, suggesting holes are the dominant carriers. The WS_2 layer may have a high carrier density due to the photogenerated carriers caused by exposure to sunlight. A possible reason for the slight variation in $1/C^2$ is the presence of deep states in the absorber layer, which are localized. The deep states do not have a considerable effect; therefore, the modulation of majority carriers is the primary cause of the observed impact.[67]

Fig. 9(c) illustrates the capacitance–voltage (C–V) properties of a solar cell based on WS_2 carrier concentration. The capacitance changes with increasing doping concentration of the absorber layer. As the forward bias voltage increases, the capacitance values increase and function sublinearly as Mott–Schottky junctions. The Mott–Schottky plot under AM 1.5G sunlight illumination indicated a lower built-in potential, which could be attributed to the capacitance generated by photogenerated carriers within photoactive materials. An earlier study reported that the increase in doping density leads to an increase in charge accumulation at the interface, which in turn results in an improvement in capacitance.[69] In Fig. 9(d), the graph shows the relationship between capacitance and bias voltage at different absorber thicknesses at a constant frequency of 1 MHz. The change in capacitance with thickness variation shows an almost linear relation. However, after the voltage of 0.70 V, a significant rise in capacitance value is observed with the increase in voltage. Thus, the WS_2 absorber has the potential to design high-efficiency photovoltaics with significant C–V behavior.

3.7 Influence of operating temperature on the performance of the solar cell

Fig. 10 illustrates the impact of operating temperatures on photovoltaic parameters of the proposed WS_2-based solar cells for both configurations, with and without the BSF layer. The stability of the PV cell could be explored by the investigation of operating temperatures ranging from 275 to 475 K. A drastic reduction in PV parameters is observed for both WS_2-based heterojunctions with and without V_2O_5 BSF when the working temperature rises from 275 to 475 K. The PCE decreased from 33.19% to 23.27% and from 24.56% to 15.75% as the operating temperature increased from 275 to 475 K for heterostructures with and without BSF, respectively. An increase in operating temperature leads to the shrinking of the band gap of WS_2 and an increase in the reverse saturation current.[70] As a result, the values of V_{OC}, FF, and consequently the cell efficiency were affected noticeably at higher working temperatures. The declination in power conversion efficiency at higher operating temperatures observed in this study is consistent with previous reports.[40,71–74]

3.8 Performance of the device output

Fig. 11 displays the current density–voltage (J–V) characteristics of the WS_2-based TFSCs. From Fig. 11, it is evident that the

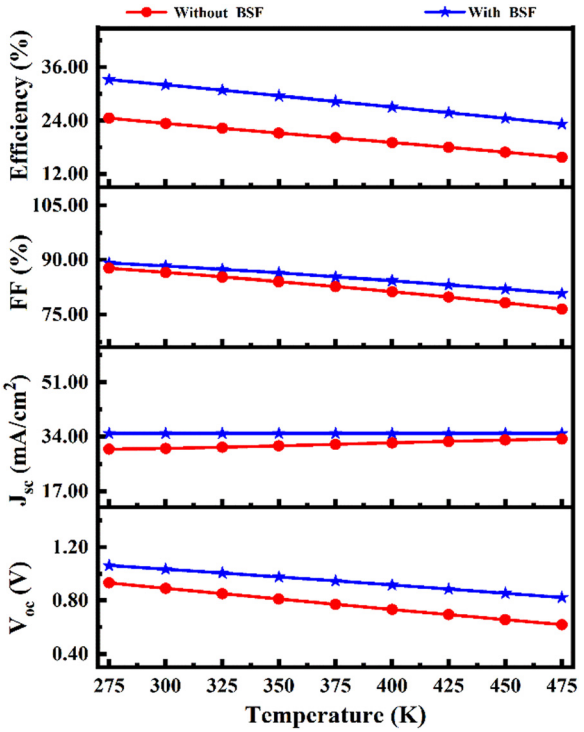

Fig. 10 Effect of temperature on the PV parameters of the solar cell.

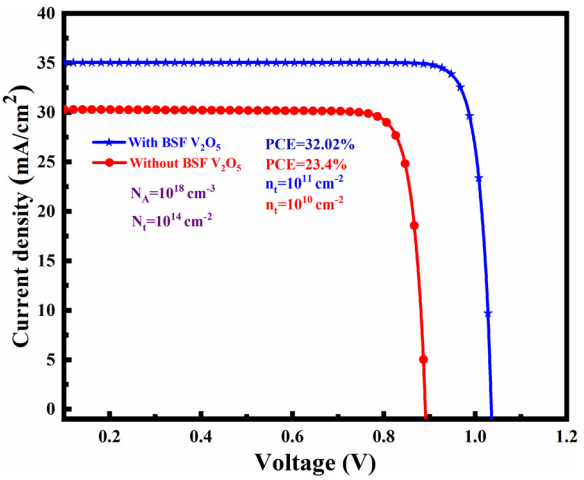

Fig. 11 J–V characteristics of the WS_2-based solar cells.

Al/FTO/SnS_2/WS_2/V_2O_5/Ni heterojunction solar cell exhibits a notably superior estimated current density compared to the reference WS_2-based heterojunction solar cell, Al/FTO/SnS_2/WS_2/Ni. Without BSF, the WS_2-based solar cell achieves a V_{OC} of 0.89 V, J_{SC} of 31.2 mA cm^{-2}, FF of 81.0%, and power conversion efficiency of 23.4%. On the other hand, the configuration with BSF results in a V_{OC} of 1.1 V, J_{SC} of 37.2 mA cm^{-2}, FF of 84.0%, and efficiency of 32.02%. The solar cell with BSF configuration achieves improved electrical device outputs in terms of V_{OC} and J_{SC} (as observed from the J–V analysis). This enhancement leads to an overall increase in the power conversion efficiency of the solar cell. Therefore, the inclusion of V_2O_5

Table 3 Summary of the reported experimental and theoretical work

Sl No	Type	Cell structure	Cell thickness (μm)	V_{OC} (V)	J_{SC} (mA cm^{-2})	FF (%)	η (%)	Ref.
1	E	ZnO/WS_2		0.362	0.65	41.1	1.7	33
2	E	ITO/WS_2		0.551	1.01	47.6	3.9	33
3	E	FTO/dye/WSG2		0.79	18.6	66	9.6	77
4	T	$ZnO/SnS_2/CZTS/MoS_2$	0.08/0.05/1.5/0.1	0.7178	26.9976	65.67	12.73	52
5	T	$ZnO/ZnSe/WS_2/Mg$	0.03/0.045/2.5/0.05	0.9	25	85	20	78
6	T	$ITO/WS_2/CdS/Sb_2Se_3$	0.025/0.05/0.06/0.4	0.706	40.52	72	20.6	79
7	T	SnO_2: F(FTO)/WS_2/Cu_2Te	0.05/0.05/1.0	0.68	42.95	82.77	24.23	80
8	T	ZnO: Al/ZnO/WS_2	0.2/0.05/2	0.90	32.70	86.5	25.71	35
9	T	Spiro-OMeTAD/$CH_3NH_3PbI_3/WS_2$	0.1/0.35/0.15	1.056	25.483	88.54	25.70	81
10	T	FTO/n-WS_2/Sb_2S_3	0.05/0.03/1.2	1.23	26.6	89.60	26.60	10
11	T	FTO/n-WS_2/Sb_2Se_3	0.05/0.03/1.2	0.85	38.40	86.56	28.20	10
12	T	n-ZnO/n-CdS/p-WS_2	0.2/0.05/2	0.8872	39.34	84.93	29.64	82
13	T	FTO/CdS/WS_2	0.05/0.05/1.0*	0.83	31.88	83.66	22.09	13
14	T	FTO/CdS/WS_2/CuI	0.05/0.05/1.0*/0.1	0.98	35.19	87.08	29.87	13
15	T	FTO/SnS_2/WS_2	0.05/0.05/1.0	0.89	31.2	81	23.4	**
16	T	FTO/$SnS_2/WS_2/V_2O_5$	0.05/0.05/1.0/0.1	1.1	37.2	84	32.02	**

Note that * means this work, T = theoretical, and E = experimental.

as a BSF layer is suggested to significantly enhance the performance of the proposed WS_2-based solar cell. In earlier experiments, CdS was used as buffer layer, which is toxic; here, SnS_2 was used instead of CdS, being nontoxic and readily available.[13,52] Table 3 presents a comparative overview of the advantages brought about by the incorporation of V_2O_5 BSF in WS_2 solar cells, along with its positive impacts when compared to analogous materials. The TFSCs proposed in this study could be more commercially attractive than other structures mentioned in Table 3.

In double heterostructures, with the insertion of a BSF layer like V_2O_5, the sub-bandgap photons may get absorbed significantly, specifically in the longer wavelength, which results in the improvement in photovoltaic performance. The sub-bandgap photons may be absorbed by the Urbach energy states, and these lower energy sub-bandgap photons participate in tail-state-assisted (TSA) two-step photon upconversion. These absorbed photons generate additional electron–hole pairs, resulting in a noticeable improvement in cell photocurrent. With the assistance of Urbach tail states, two sub-bandgap photons are absorbed in a row in this process. However, the degree of upconversion and the resulting enhancement in photocurrent depends on the Urbach energy, E_0, of the photoactive material. This TSA upconversion takes place in a photoactive material when it possesses adequate doping concentration, high absorption coefficient and favorable bandgap.[75,76] The higher Urbach energy significantly contributes to enhancing the quantum efficiency (QE), specifically in the longer wavelength.[48–51,76] The equation for Urbach energy is shown in eqn (8). Thus, the authors believe that enhanced PV performance can be obtained in the proposed double-junction solar cells with relevant modelling and the convincing simulation parameter data.

$$\alpha = \alpha_0 \exp(E/E_u), \quad (8)$$

where α is the absorption coefficient, α_0 is a constant, E is the photon energy, and E_u is the Urbach energy. The Urbach energy is calculated from inverse of $\ln \alpha$ *vs.* E slope.

4. Conclusions

Through numerical modeling with a SCAPS-1D simulator, high-efficiency transition metal dichalcogenide thin-film heterojunction solar cells with SnS_2 buffer and V_2O_5 BSF layers have been explored. Potential V_2O_5 BSF and SnS_2 buffer layer materials with the required layer properties, such as thickness, carrier doping concentration, and defect densities, have been investigated and adjusted through a comprehensive study. The best and adjusted layer thicknesses for the SnS_2 buffer, WS_2 absorber, and V_2O_5 BSF layer were found to be 0.05, 1.0, and 0.10 μm, respectively, with a bulk defect density of 10^{14} cm^{-3}, and the interface defect densities of 10^{11} cm^{-2} at WS_2/V_2O_5 and 10^{10} cm^{-2} at WS_2/SnS_2 were determined. These results indicate that the addition of a V_2O_5 BSF to the reference SnS_2/WS_2 TFSCs offers an efficient dual-heterojunction solar cell showing the improved (by almost 9%) PCE of 32.02% with V_{OC} of 1.1 V, J_{SC} of 37.2 mA cm^{-2} and FF of 84% for the Al/FTO/$SnS_2/WS_2/V_2O_5$/Ni heterostructure, compared to the PCE of 23.4% with V_{OC} of 0.89V, J_{SC} of 31.2 mA cm^{-2} and FF of 81% in the reference cell. The proposed WS_2 cell has been shown to have better stability and performance than the reference WS_2 solar cell. The results show the enormous potential of the $SnS_2/WS_2/V_2O_5$ heterostructure for designing and manufacturing high-efficiency photovoltaic cells and open a clear path for the production of WS_2-based photovoltaic and photonic devices based on transition-metal dichalcogenides.

Author contributions

Md. Ferdous Rahman and Abdul Kuddus: conceptualization, methodology, software, validation, formal analysis, visualization, investigation, data curation, supervision, writing – original draft, review & editing. Jubair Al Mahmud: methodology, software, validation, formal analysis, visualization investigation, data curation, writing – original draft, review & editing. Md. Hasan Ali, A. T. M. Saiful Islam, Md Dulal Haque, Sheikh Rashel Al Ahmed, Muhammad Mushtaq, Abu Bakar Md. Ismail:

validation, formal analysis, writing – original draft, review & editing.

Ethical approval

All authors declare that the manuscript does not have studies on human subjects, human data or tissue, or animals.

Conflicts of interest

The authors have no conflicts of interest.

Acknowledgements

The authors would like to offer their heartfelt appreciation to Dr Marc Burgelman and his colleagues at the EIS Department at the University of Gent in Belgium for providing the opportunity to use the SCAPS-1D software. The authors are also grateful to the Department of Electrical and Electronic Engineering, Begum Rokeya University, Rangpur 5400, Bangladesh, for the use of the Advanced Energy Materials and Solar Cell Research Laboratory.

References

1 M. H. Ali, M. A. Al Mamun, M. D. Haque, M. F. Rahman, M. K. Hossain and A. Z. M. T. Islam, *ACS Omega*, 2023, **8**, 7017–7029.
2 M. F. Rahman, J. Hossain, A. Kuddus, S. Tabassum, M. H. K. Rubel, M. M. Rahman, Y. Moriya, H. Shirai and A. B. M. Ismail, *J. Mater. Sci.*, 2020, **55**, 7715–7730.
3 A. Isha, A. Kowsar, A. Kuddus, M. K. Hossain, M. H. Ali, M. D. Haque and M. F. Rahman, *Heliyon*, 2023, **9**, e15716.
4 A. Tolón-Becerra, X. Lastra-Bravo and F. Bienvenido-Bárcena, *Renewable Energy*, 2011, **36**, 2067–2077.
5 M. K. Hossain, A. A. Arnab, R. C. Das, K. M. Hossain, M. H. K. Rubel, M. F. Rahman, H. Bencherif, M. E. Emetere, M. K. A. Mohammed and R. Pandey, *RSC Adv.*, 2022, **12**, 34850–34873.
6 M. K. Hossain, M. K. A. Mohammed, R. Pandey, A. A. Arnab, M. H. K. Rubel, K. M. Hossain, M. H. Ali, M. F. Rahman, H. Bencherif, J. Madan, M. R. Islam, D. P. Samajdar and S. Bhattarai, *Energy Fuels*, 2023, **37**, 6078–6098.
7 M. K. Hossain, S. Bhattarai, A. A. Arnab, M. K. A. Mohammed, R. Pandey, H. Ali, F. Rahman, R. Islam, D. P. Samajdar, J. Madan, H. Bencherif, D. K. Dwivedi and M. Amami, *RSC Adv.*, 2023, **13**, 21044–21062.
8 M. F. Rahman, N. Mahmud, I. Alam, M. H. Ali, M. M. A. Moon, A. Kuddus, G. F. I. Toki, M. H. K. Rubel, M. A. Al Asad and M. K. Hossain, *AIP Adv.*, 2023, **13**, 045309.
9 M. Aghaei, Y. H. M. Thayoob, M. Imamzai, P. Piyous and N. Amin, *2013 IEEE 7th International Power Engineering and Optimization Conference (PEOCO)*, IEEE, 2013, pp. 203–208.
10 M. F. Rahman, M. M. Alam Moon, M. K. Hossain, M. H. Ali, M. D. Haque, A. Kuddus, J. Hossain and A. B. Abu, *Heliyon*, 2022, **8**, e12034.
11 S. Ahmmed, A. Aktar, S. Tabassum, M. H. Rahman, M. F. Rahman and A. B. Abu, *Superlattices Microstruct.*, 2021, **151**, 106830.
12 M. F. Rahman, M. J. A. Habib, M. H. Ali, M. H. K. Rubel, M. R. Islam, A. B. Abu and M. K. Hossain, *AIP Adv.*, 2022, **12**, 1–11.
13 M. M. Khatun, A. Sunny and S. R. Al Ahmed, *Sol. Energy*, 2021, **224**, 956–965.
14 N. R. Paudel, K. A. Wieland and A. D. Compaan, *Solar Energy Mater. Solar Cells*, 2012, **105**, 109–112.
15 M. Powalla, S. Paetel, E. Ahlswede, R. Wuerz, C. D. Wessendorf and T. Magorian Friedlmeier, *Appl. Phys. Rev.*, 2018, **5**, 041602.
16 C.-T. Lee, K.-F. Lu and C.-Y. Tseng, *Sol. Energy*, 2015, **114**, 1–7.
17 A. Hu, J. Zhou, P. Zhong, X. Qin, M. Zhang, Y. Jiang, X. Wu and D. Yang, *Sol. Energy*, 2021, **214**, 319–325.
18 M. Nakamura, K. Yamaguchi, Y. Kimoto, Y. Yasaki, T. Kato and H. Sugimoto, *IEEE J. Photovolt.*, 2019, **9**, 1863–1867.
19 C. Candelise, M. Winskel and R. Gross, *Prog. Photovoltaics Res. Appl.*, 2012, **20**, 816–831.
20 L. A. Kosyachenko, X. Mathew, P. D. Paulson, V. Y. Lytvynenko and O. L. Maslyanchuk, *Solar Energy Mater. Solar Cells*, 2014, **130**, 291–302.
21 N. Asim, K. Sopian, S. Ahmadi, K. Saeedfar, M. A. Alghoul, O. Saadatian and S. H. Zaidi, *Renewable Sustainable Energy Rev.*, 2012, **16**, 5834–5847.
22 D. J. Xue, B. Yang, Z. K. Yuan, G. Wang, X. Liu, Y. Zhou, L. Hu, D. Pan, S. Chen and J. Tang, *Adv. Energy Mater.*, 2015, **5**, 1–9.
23 T. M. Razykov, G. S. Boltaev, A. Bosio, B. Ergashev, K. M. Kouchkarov, N. K. Mamarasulov, A. A. Mavlonov, A. Romeo, N. Romeo, O. M. Tursunkulov and R. Yuldoshov, *Sol. Energy*, 2018, **159**, 834–840.
24 E. S. Hossain, P. Chelvanathan, S. A. Shahahmadi, K. Sopian, B. Bais and N. Amin, *Curr. Appl. Phys.*, 2018, **18**, 79–89.
25 M. W. Iqbal, M. Z. Iqbal, M. F. Khan, M. A. Shehzad, Y. Seo, J. H. Park, C. Hwang and J. Eom, *Sci. Rep.*, 2015, **5**, 1–9.
26 A. Matthäus, A. Ennaoui, S. Fiechter, S. Tiefenbacher, T. Kiesewetter, K. Diesner, I. Sieber, W. Jaegermann, T. Tsirlina and R. Tenne, *J. Electrochem. Soc.*, 1997, **144**, 1013–1019.
27 S.-Y. Chen, C. Zheng, M. S. Fuhrer and J. Yan, *Nano Lett.*, 2015, **15**, 2526–2532.
28 A. Jager-Waldau, M. C. Lux-Steiner, E. Bucher and G. Jager-Waldau, in Conference Record of the Twenty Third IEEE Photovoltaic Specialists Conference – 1993 (Cat. No. 93CH3283-9), IEEE, pp. 597–602.
29 S. Roy and P. Bermel, *Solar Energy Mater. Solar Cells*, 2018, **174**, 370–379.
30 R. Chaurasiya, G. K. Gupta and A. Dixit, *Solar Energy Mater. Solar Cells*, 2019, **201**, 110076.

31 K. Nassiri Nazif, A. Kumar, M. T. Moreira de Menezes and K. Saraswat, in *Wide Bandgap Materials, Devices, and Applications IV*, ed. M. Matin, A. K. Dutta and A. P. Lange, SPIE, 2019, p. 7.
32 C. Ballif, M. Regula, F. Lévy, F. Burmeister, C. Schäfle, T. Matthes, P. Leiderer, P. Niedermann, W. Gutmannsbauer and R. Bucher, *J. Vac. Sci. Technol., A*, 1998, **16**, 1239–1243.
33 A. Jäger-Waldau, M. C. Lux-Steiner and E. Bucher, *Solid State Phenom.*, 1994, **37–38**, 479–484.
34 A. K. Patel and B. P. Pandey, *2020 International Conference on Electrical and Electronics Engineering (ICE3)*, IEEE, 2020, pp. 382–384.
35 K. Sobayel, K. S. Rahman, M. R. Karim, M. O. Aijaz, M. A. Dar, M. A. Shar, H. Misran and N. Amin, *Chalcogenide Lett.*, 2018, **15**, 307–315.
36 K. Ellmer, *Phys. Status Solidi B*, 2008, **245**, 1745–1760.
37 A. T. Nguyen, J. Wang, E. Cho, S. Lim, S. Kwon, J. Song, K. Zhou and D. W. Kim, *Adv. Mater. Interfaces*, 2023, **2300031**, 1–7.
38 A. K. Singh, R. Walia, M. S. Chauhan, R. S. Singh and V. K. Singh, *Environ. Sci. Pollut. Res.*, 2022, DOI: **10.1007/s11356-022-24236-6**.
39 A. Ahmed, K. Riaz, H. Mehmood, T. Tauqeer and Z. Ahmad, *Opt. Mater.*, 2020, **105**, 109897.
40 S. R. Al Ahmed, A. Sunny and S. Rahman, *Solar Energy Mater. Solar Cells*, 2021, **221**, 110919.
41 M. K. Hossain, G. F. I. Toki, A. Kuddus, M. K. A. Mohammed, R. Pandey, J. Madan, S. Bhattarai, F. Rahman, D. K. Dwivedi, M. Amami, H. Bencherif and D. P. Samajdar, *Mater. Chem. Phys.*, 2023, **308**, 128281.
42 S. Z. Haider, H. Anwar, Y. Jamil and M. Shahid, *J. Phys. Chem. Solids*, 2020, **136**, 109147.
43 T. Minemoto and M. Murata, *Solar Energy Mater. Solar Cells*, 2015, **133**, 8–14.
44 Y. Cao, X. Zhu, H. Chen, X. Zhang, J. Zhouc, Z. Hu and J. Pang, *Solar Energy Mater. Solar Cells*, 2019, **200**, 109945.
45 A. Kuddus, M. F. Rahman, J. Hossain and A. B. M. Ismail, *EPJ Appl. Phys.*, 2020, **92**, 1–14.
46 L. Zhang, C. Jiang, C. Wu, H. Ju, G. Jiang, W. Liu, C. Zhu and T. Chen, *ACS Appl. Mater. Interfaces*, 2018, **10**, 27098–27105.
47 M. Burgelman, P. Nollet and S. Degrave, *Thin Solid Films*, 2000, **361–362**, 527–532.
48 M. S. Chowdhury, S. A. Shahahmadi, P. Chelvanathan, S. K. Tiong, N. Amin, K. Techato, N. Nuthammachot, T. Chowdhury and M. Suklueng, *Results Phys.*, 2020, **16**, 102839.
49 A. Ait Abdelkadir, E. Oublal, M. Sahal and A. Gibaud, *Results Opt.*, 2022, **8**, 100257.
50 S. Ahmmed, A. Aktar, M. F. Rahman, J. Hossain and A. B. M. Ismail, *Optik*, 2020, **223**, 165625.
51 A. Kuddus, M. F. Rahman, S. Ahmmed, J. Hossain and A. B. M. Ismail, *Superlattices Microstruct.*, 2019, **132**, 106168.
52 F. Belarbi, W. Rahal, D. Rached, S. Benghabrit and M. Adnane, *Optik*, 2020, **216**, 164743.
53 M. Haghighi, M. Minbashi, N. Taghavinia, D. H. Kim, S. M. Mahdavi and A. A. Kordbacheh, *Sol. Energy*, 2018, **167**, 165–171.
54 S. Roy and P. Bermel, *Solar Energy Mater. Solar Cells*, 2018, **174**, 370–379.
55 A. Niemegeers, M. Burgelman and K. Decock, *SCAPS Manual*.
56 A. I. Likhter, E. G. Pel and S. I. Prysyazhnyuk, *Phys. Status Solidi A*, 1972, **14**, 265–270.
57 M. F. Rahman, M. J. A. Habib, M. H. Ali, M. H. K. Rubel, M. R. Islam, A. B. M. Ismail and M. K. Hossain, *AIP Adv.*, 2022, **12**, 105317.
58 M. A. Matin, M. U. Tomal, A. M. Robin and N. Amin, *Int. J. Photoenergy*, 2013, **2013**, 652695.
59 M. M. A. Moon, M. F. Rahman, M. Kamruzzaman, J. Hossain and A. B. M. Ismail, *Energy Rep.*, 2021, **7**, 1742–1756.
60 M. K. Hossain, M. H. K. Rubel, G. F. I. Toki, I. Alam, M. F. Rahman and H. Bencherif, *ACS Omega*, 2022, **7**, 43210–43230.
61 M. M. A. Moon, M. H. Ali, M. F. Rahman, A. Kuddus, J. Hossain and A. B. M. Ismail, *Phys. Scr.*, 2020, **95**, 035506.
62 S. Kohnehpoushi, P. Nazari, B. A. Nejand and M. Eskandari, *Nanotechnology*, 2018, **29**, 205201.
63 M. Atowar Rahman, *Sol. Energy*, 2021, **215**, 64–76.
64 Y. H. Khattak, F. Baig, S. Ullah, B. Marí, S. Beg and H. Ullah, *J. Renewable Sustainable Energy*, 2018, **10**, 033501.
65 R. K. Zahoo and A. N. Saleh, *Turkish Journal of Computer and Mathematics Education*, 2021, **12**, 5056–5064.
66 F. Ferdiansjah and K. Tirtakusuma Mularso, *E3S Web of Conferences*, 2018, **43**, 01006.
67 G. K. Gupta, A. Garg and A. Dixit, *J. Appl. Phys.*, 2018, **123**, 013101.
68 M. H. Ali, M. A. Al Mamun, M. D. Haque, M. F. Rahman, M. K. Hossain and A. Z. M. Touhidul Islam, *ACS Omega*, 2023, **8**, 7017–7029.
69 M. Samiul Islam, K. Sobayel, A. Al-Kahtani, M. A. Islam, G. Muhammad, N. Amin, M. Shahiduzzaman and M. Akhtaruzzaman, *Nanomaterials*, 2021, **11**, 1218.
70 P. Singh and N. M. Ravindra, *Solar Energy Mater. Solar Cells*, 2012, **101**, 36–45.
71 A. Bouich, B. Hartiti, S. Ullah, H. Ullah, M. E. Touhami, D. M. F. Santos and B. Mari, *Optik*, 2019, **183**, 137–147.
72 A. Sunny and S. R. Al Ahmed, *Phys. Status Solidi B*, 2021, **258**, 2000630.
73 S. R. I. Biplab, M. H. Ali, M. M. A. Moon, M. F. Pervez, M. F. Rahman and J. Hossain, *J. Comput. Electron.*, 2020, **19**, 342–352.
74 H. I. Abdalmageed, M. Fedawy and M. H. Aly, *J. Phys.: Conf. Ser.*, 2021, **2128**, 012009.
75 A. Kuddus, S. K. Mostaque and J. Hossain, *Opt. Mater. Express*, 2021, **11**, 3812.
76 S. Khaled Mostaque, B. Kumar Mondal and J. Hossain, *Results Opt.*, 2022, **8**, 100250.
77 D. Krishnamoorthy and A. Prakasam, *J. Cluster Sci.*, 2021, **32**, 621–630.
78 S. Khan, M. Rashid, W. Rahim, M. Aitezaz Hussain and A. Rahim, *Int. J. Eng. Works*, 2020, **07**, 149–153.

79 S. Naureen, S. Rai, R. K. Yadav, P. Lohia and D. K. Dwivedi, *Opt. Quantum Electron.*, 2023, **55**, 541.
80 S. R. Al Ahmed, M. Rahaman, A. Sunny, S. Rahman, M. Saiful Islam, T. Abd El-Mohaymen Taha, Z. A. Alrowaili and M. Suruz Mian, *Opt. Laser Technol.*, 2023, **159**, 108942.
81 K. Sobayel, M. Akhtaruzzaman, K. S. Rahman, M. T. Ferdaous, Z. A. Al-Mutairi, H. F. Alharbi, N. H. Alharthi, M. R. Karim, S. Hasmady and N. Amin, *Results Phys.*, 2019, **12**, 1097–1103.
82 A. K. Patel and B. P. Pandey, *Int. Conf. Electr. Electron. Eng.*, 2020, 382–384.